Sustainable synthesis of structurally robust $LiNi_{1/3}Mn_{1/3}Co_{1/3}O_2$ cathodes with enhanced electrochemical performance

T. Kiruthika[a+], C. Choi[b+], D. Lakshmi[c], T. Surya Prabha[b], Ki Ro Yoon[d], P. Sakthivel[e], Byungil Hwang[f], P Christopher Selvin[a*]*

[a]*Department of Physics, Bharathiar University, Coimbatore-46, Tamilnadu, India*

[b]*Department of Intelligent Semiconductor Engineering, Chung-Ang University, Seoul 06974, Republic of Korea*

[c]*Department of Physics, PSG College of Arts and Science, Coimbatore-14, Tamilnadu, India*

[d]*Textile Innovation R&D Department, Korea Institute of Industrial Technology143, Sangnok-gu, Ansan-si, Republic of Korea*

[e]*Department of Nanoscience and Technology, Bharathiar University, Coimbatore-46, Tamilnadu, India*

[f]*School of Integrative Engineering, Chung-Ang University, Seoul 06974, Republic of Korea*

Corresponding authors

Email address: csphysics@buc.edu.in, bihwang@cau.ac.kr,

+These authors contributed equally to this work.

Abstract

This study reports on the green synthesis of high-performance $LiNi_{1/3}Mn_{1/3}Co_{1/3}O_2$ (NMC111) cathode materials using *Actinidia deliciosa* (kiwi) extract as a natural chelating and reducing agent. The electrochemical and structural performance of the green-synthesized NMC (GS-NMC) was systematically compared with NMCs prepared using sol–gel and solid-state methods. Structural and surface analyses show that GS-NMC possesses a highly ordered layered structure with minimal cation mixing, improved crystallinity, and increased surface area. Electron microscopy and BET analyses confirm a refined nanoscale morphology with well-developed porosity. The XPS results indicate reduced surface impurities and an optimal distribution of transition-metal oxides. Electrochemical testing in a three-electrode aqueous LiOH system demonstrates that GS-NMC achieves enhanced surface redox activity, low

interfacial resistance, and stable pseudocapacitive behavior (approximately 120 $mAh \cdot g^{-1}$ within a ±0.3 V window) over 1000 cycles. In comparison, sol–gel and solid-state samples exhibit higher polarization and faster capacity fading. Although tested under aqueous half-cell conditions, the results show that green synthesis offers a promising route to produce structurally robust and electrochemically responsive NMC materials. The findings also highlight the promise of biogenic synthesis as a sustainable alternative to traditional methods and as a versatile platform for designing high performed cathode materials for next generation lithium-ion batteries.

Keywords: Green synthesis, $LiNi_{1/3}Mn_{1/3}Co_{1/3}O_2$, Kiwi extract, Cathode materials, Electrochemical performance, Aqueous lithium-ion batteries.

Introduction

Layered lithium nickel manganese cobalt oxide ($LiNi_{1/3}Mn_{1/3}Co_{1/3}O_2$, commonly referred to as NMC111) is one of the most widely studied cathode materials for lithium-ion batteries due to its high reversible capacity and balanced energy density [1-4]. However, its electrochemical performance depends strongly on the synthesis route, which determines particle size, crystallinity, and cation ordering within the lattice[5,6]. The layered structure of NMC is particularly susceptible to Li^+/Ni^{2+} cation mixing when the material is synthesized under suboptimal conditions. This cation disorder (where Ni^{2+} partially occupies Li^+ sites) is thermodynamically favorable but electrochemically detrimental because it hinders Li^+ diffusion and compromises both rate capability and cycle life[5]. Therefore, a key goal in cathode preparation is to minimize Ni/Li disorder and obtain a well-ordered R-3m layered phase with high structural integrity[5, 7].

Conventional synthesis methods for NMC include co-precipitation, sol–gel, and solid-state

reactions[8-11]. The solid-state method typically involves high-temperature calcination of mixed oxide or carbonate precursors and is favored for its simplicity and scalability [12, 13]. However, solid-state routes often require prolonged heating, which can lead to lithium loss (via Li_2O evolution) and the formation of impurity phases such as Li_2CO_3 on particle surfaces. These conditions also promote grain growth, which can result in larger particles with lower surface area and longer Li^+ diffusion paths. Sol–gel synthesis, in contrast, uses organic chelating and fueling agents (e.g., citric acid) to bind metal ions in solution and to produce a homogeneous gel that converts to the oxide at moderate temperatures[8, 14]. Sol–gel methods can produce materials with excellent compositional uniformity and smaller particle sizes, and they allow for the tailoring of morphology through processing parameters10, 15. For example, Kızıltaş-Yavuz et al.[16] synthesized NMC111 using table sugar as a chelating and fuel agent in a sol–gel process, achieving phase-pure layered NMC with sub-micron spherical particles and a capacity of approximately 149 $mAh \cdot g^{-1}$. Nonetheless, even sol–gel methods rely on chemical additives and often require multiple steps or expensive reagents. There is increasing interest in more sustainable, "green" synthesis approaches that minimize the use of hazardous chemicals and lower energy consumption during cathode production.

Plant extracts have recently been investigated as green precursors for synthesizing inorganic nanomaterials due to their high content of organic acids, polyphenols, and sugars, which can serve as natural chelating and reducing agents[17-19]. Utilizing plant-derived compounds can enable an eco-friendly combustion-type synthesis where the plant extract serves as a renewable fuel for the thermal decomposition of metal salts. Such bio-mediated processes align with solution combustion methods (also known as self-combustion or sol–gel combustion), which are known to produce highly crystalline, homogeneous oxides rapidly via

an exothermic reaction of an oxidizer (metal nitrates) and a fuel (organic compounds, such as citric acid or urea)[8, 20]. When selecting a suitable bio-extract, one considers factors analogous to those of classic fuels, including the abundance of functional groups and complex metal ions, high oxygen content, and low toxicity for efficient combustion, as well as benign decomposition by-products. *Actinidia deliciosa* (kiwi fruit) extract meets these criteria, containing organic acids (e.g., ascorbic acid), sugars, and amino acids that can chelate metal cations and facilitate their co-precipitation, as well as combust upon heating to yield fine oxide powders[21, 22]. Kiwi and other fruit extracts have already been successfully used to synthesize various metal oxides and nanoparticles as a greener alternative to traditional chemical routes[17, 23]. The use of kiwi extract in NMC synthesis is expected not only to be environmentally benign but also to confer unique advantages in particle morphology (through the templating effect of biomolecules) and surface chemistry (possible *in-situ* surface passivation or carbon doping from organic residues).

In this work, we investigate NMC111 cathodes prepared via a kiwi extract-assisted green synthesis and directly compare them with NMC prepared using a conventional sol–gel method (using citric acid) and a solid-state method. The aim is to elucidate how the green route affects the crystallographic order, particle microstructure, and surface electrochemical properties of NMC. All three materials are subjected to identical characterization and *aqueous* electrochemical testing. While lithium-ion cathodes are typically evaluated in non-aqueous full cells, we use a three-electrode cell with 1 M LiOH aqueous electrolyte to probe the redox behavior and interfacial kinetics of the NMC samples in a controlled manner. Aqueous electrolytes offer advantages in terms of safety, low cost, and high ionic conductivity (approximately 10^{-1} $S \cdot cm^{-1}$) [24-27], and they allow rapid screening of electrode performance

without the complexities of full battery assembly. However, the narrow electrochemical stability window of water (approximately 1.23 V) fundamentally limits the voltage range accessible to the cathode. The primary Li^+ intercalation reactions of NMC occur at approximately 3–4.3 V versus Li^+/Li, which lies well outside the water stability window. As a result, direct measurement of the material's theoretical capacity in aqueous media is not possible. Instead, the electrochemical response in 1 M LiOH primarily reflects near-surface redox processes, such as the Ni(II)/Ni(III) couple (analogous to the $Ni(OH)_2$/NiOOH conversion, typically occurring around 0.4–0.5 V vs Hg/HgO in alkaline solution), and capacitive charge storage at the interface. Despite these limitations, aqueous testing can be informative for comparing the charge-transfer resistance, cyclability, and structural stability of different NMC materials under accelerated conditions [28-30]. Prior studies have shown that trends observed in three-electrode half-cell tests (e.g., lower impedance or better stability for a given sample) often translate to improved performance in real-life batteries. Furthermore, demonstrating robust cycling in an aqueous environment (which is intrinsically more hostile due to transition-metal dissolution and the absence of protective SEI layers) is a strong indication of a structurally resilient cathode.

In this work, we emphasize the structural and surface electrochemical benefits of green synthesis. The GS-NMC is found to maintain a well-layered structure with reduced cation-mixing and microstrain, possesses a higher surface area and porosity for electrolyte penetration, and exhibits lower charge-transfer resistance in our tests. We discuss how these factors make GS-NMC a promising candidate for lithium-ion battery cathodes, although full-cell evaluation remains necessary for quantifying metrics such as energy density. This study critically examines the use of an aqueous three-electrode system and recognizes both its limitations and

its value for the initial screening of novel cathode materials. The results highlight an often-overlooked connection between synthesis chemistry and electrochemical behavior, and they show that a green, bio-assisted synthesis produces NMC cathodes with significant performance enhancements.

Experimental Section

Green synthesis of NMC using kiwi extract: Nickel(II) nitrate hexahydrate [$Ni(NO_3)_2 \cdot 6H_2O$], manganese (II) nitrate tetrahydrate [$Mn\ (NO_3)_2 \cdot 4H_2O$], and cobalt (II) nitrate hexahydrate [$Co(NO_3)_2 \cdot 6H_2O$] served as precursor salts for Ni, Mn, and Co, respectively. A fresh kiwi fruit (*Actinidia deliciosa*) was peeled and blended with deionized water to prepare the extract. The extract was then filtered to remove solid pulp. The resulting solution acted as both a chelating agent and a fuel, and it was added to an aqueous mixture of Ni, Mn, and Co nitrates in a molar ratio of 1:1:1. A slight excess of lithium precursor (added separately, as described below) was included to compensate for lithium loss during calcination. The pH of the mixture was adjusted to approximately 7 using a mild base, which facilitated the complexation of metal ions with the bioactive components of the extract. The solution was heated to approximately 80 °C under continuous stirring for about 3 hours. A viscous gel gradually formed through evaporation and bio-mediated ion binding ("green gelation"). The gel was dried at 120 °C to obtain a precursor powder and calcined in air at 700 °C for 5 hours with a ramp rate of about 5 $°C \cdot min^{-1}$. During calcination, the organic components decomposed through self-combustion, which produced crystalline $LiNi_{1/3}Mn_{1/3}Co_{1/3}O_2$. The resulting product was cooled naturally to room temperature and gently ground to break up agglomerates. This sample is referred to as GS-NMC (green-synthesized NMC).

Sol–gel synthesis of NMC: For comparison, NMC was synthesized using a citric acid sol–gel

method. Nickel, manganese, and cobalt nitrates (in a 1:1:1 molar ratio for Ni:Mn:Co) were dissolved in deionized water. Citric acid, which acted as both a chelating agent for the metal ions and as a combustion fuel, was added to the solution at a molar ratio of approximately 1.5:1. The solution was heated to about 80 °C under stirring for approximately 5 hours. During this process, the solution underwent dehydration and formed a gel. A pinkish gel formed as the water evaporated, and metal–citrate complexes developed. This gel was dried at 120 °C to yield a xerogel precursor. The dry precursor was calcined at 700 °C for 17 hours in the air. The resulting lithium nickel manganese cobalt oxide powder was collected. The obtained powder was ground thoroughly for 1 hour and subsequently heated to 700 °C for 3 hours to enhance crystallinity This sample is referred to as SG-NMC (sol–gel NMC).

Solid-state synthesis of NMC: In the solid-state route, stoichiometric amounts of $Ni(NO_3)_2$, $Mn(NO_3)_2$, and $Co(NO_3)_2$ (for Ni:Mn:Co = 1:1:1) were first converted to their corresponding carbonate or hydroxide intermediates by precipitation. A mixed solution of nitrates was treated with a sodium carbonate solution under ambient conditions, which produced a co-precipitated Ni–Mn–Co carbonate (hydroxide) solid after filtration and washing. The obtained precursor was dried and pressed into a pellet and calcined at 700 °C for 17 hours in air (to ensure a complete reaction, given the solid–solid diffusion requirements. The resultant powder was reground and subjected to an additional heat treatment at 700 °C for 2 hours to improve phase formation. After furnace cooling, the pellet was ground into a fine powder, yielding the SS-NMC (solid-state NMC) sample. It is noted that in some alternative solid-state approaches reported in the literature, metal nitrates are directly ground with fuel and heated to combustion [8]. The overall procedures are illustrated in Figure S1.

Characterization: X-ray diffraction (XRD) analysis was carried out using a Bruker D8 Advance diffractometer equipped with Cu Kα radiation (λ = 1.5406 Å) to determine the phase composition and crystallographic structure. The XRD patterns were recorded over the 2θ range of 10°–80° with a step size of 0.02°·s^{-1}. The lattice parameters were extracted via Rietveld refinement or peak fitting, while average crystallite size and microstrain were estimated using the Scherrer equation and Williamson–Hall analysis, respectively. Fourier-transform infrared (FTIR) spectra were acquired using a Thermo Nicolet spectrometer in ATR mode over the range of 4000–500 cm^{-1} to identify residual organic and carbonate species. Raman spectroscopy was performed with a 532 nm laser excitation source (Renishaw InVia Raman microscope) in the 200–1000 cm^{-1} range to probe metal–oxygen vibrational modes and detect structural disorder. Field-emission scanning electron microscopy (FE-SEM; JEOL JSM-7600F) was used to examine surface morphology and particle size. High-resolution transmission electron microscopy (TEM; FEI Tecnai, 200 kV) and selected-area electron diffraction (SAED) were employed to examine the nanoscale structural features. Elemental mapping and compositional analysis were performed using energy-dispersive X-ray spectroscopy (EDS) coupled with SEM/TEM. Nitrogen adsorption–desorption measurements were conducted at 77 K using a Micromeritics ASAP 2020 analyzer. Prior to measurement, the samples were degassed at 120 °C for 4 hours. The specific surface area was calculated using the Brunauer–Emmett–Teller (BET) method in the relative pressure range (P/P_0) of 0.05–0.2. The pore-size distribution was derived from the desorption branch using the Barrett–Joyner–Halenda (BJH) method. X-ray photoelectron spectroscopy (XPS, PHI Quantera II with an Al Kα source) was performed to analyze the surface elemental states. High-resolution spectra for Li 1s, O 1s, C 1s, Ni 2p, Co 2p, and Mn 2p were recorded, and peak fitting was performed using CasaXPS with appropriate sensitivity factors and references (the C 1s adventitious carbon peak at 284.8

eV as an internal calibration).

Electrochemical Measurements: Electrochemical measurements were conducted in a three-electrode configuration using 1 M LiOH aqueous solution as the electrolyte. The working electrodes were prepared by mixing 80 wt% active NMC powder, 10 wt% Super P Li conductive carbon, and 10 wt% poly(vinylidene difluoride) (PVDF) binder in N-methyl-2-pyrrolidone (NMP) to form a uniform slurry. This slurry was cast onto nickel foam (for cyclic voltammetry and galvanostatic cycling) or onto glassy carbon disks (for impedance spectroscopy), followed by drying under vacuum at 80 °C. The typical mass loading of active material was approximately 2–3 $mg \cdot cm^{-2}$. A platinum mesh served as the counter electrode, and an Ag/AgCl reference electrode (in 3 M KCl) was used. Unless specified otherwise, all potentials reported are referenced against Ag/AgCl. Cyclic voltammetry (CV) was performed using a Bio-Logic VSP potentiostat by sweeping the potential from –0.5 V to +0.5 V at various scan rates (10–50 $mV \cdot s^{-1}$). The voltage window was selected to remain within the water stability limits and isolate surface redox processes while avoiding oxygen evolution typically occurring above +0.5 V. Galvanostatic charge–discharge measurements were carried out over the same potential range at constant current densities of 0.1, 0.2, 0.5, and 1 A/g, which correspond to specific currents of approximately 4, 8, 20, and 40 mAh g^{-1}, respectively, based on the typical active mass. Specific capacity ($mAh \cdot g^{-1}$) was calculated from the discharge curve by integrating the delivered charge and normalizing it by the mass of the active material. Long-term cycling performance was assessed by repeated charge–discharge tests at a fixed current (e.g., 0.5 A/g) for up to 1000 cycles (with charge and discharge capacities) as well as Coulombic efficiencies, recorded throughout. Electrochemical impedance spectroscopy (EIS) measurements were performed at open-circuit potential (OCP), which stabilized at

approximately 0 V vs Ag/AgCl for all samples in LiOH by applying a 10 mV AC perturbation over a frequency range of 100 kHz to 0.1 Hz. The Nyquist plots (–Z'' versus Z') were fitted to an equivalent circuit model (inset in Figure 5i) to extract the solution resistance (R_s) and charge-transfer resistance (R_{ct}) for each electrode. All experiments were performed at room temperature (approximately 25 °C). To evaluate structural stability after cycling, the electrodes were removed from the cell after 1000 cycles, rinsed with deionized water, and dried. The cycled NMC material was subsequently characterized by XRD (for phase analysis) and SEM (for morphology) to detect any degradation or phase transformations resulting from prolonged aqueous cycling.

Results and Discussion

Structure and phase purity of as-synthesized NMC

The XRD patterns (Cu Kα radiation) in Figure 1a confirm the formation of a layered α-$NaFeO_2$-type structure (space group R-3m) in all samples. The prominent diffraction peaks are indexed to their corresponding lattice planes, as indicated by the labeled Miller indices. The green-synthesized sample (shown in green) displays the highest relative intensity ratio of the (003) to (104) reflections and distinct splitting of the (006)/ (102) and (018)/ (110) peaks. These features indicate a highly ordered layered structure with minimal cation mixing[5]. In contrast, the sol–gel (orange) and solid-state (brown) samples exhibit slightly broader diffraction peaks, which indicates smaller crystallite sizes and/or greater lattice microstrain.

<Figure_1>

Table 1. Summary of structural and textural properties of NMC samples synthesized via sol–gel (SG), solid–state (SS), and green synthesis (GS) methods.

	Sol–gel	Solid–state	Green synthesis

Crystallite size (D, nm)	22	28	18
Strain ($\varepsilon \times 10^{-4}$)	5.34	6.91	4.28
Lattice a (Å)	2.867	2.862	2.866
Lattice c (Å)	14.218	14.206	14.198
Particle size (nm)	34	43	26
Surface area (m^2/g)	3.35	3.74	5.57
Pore diameter (nm)	40.15	29.74	37.47
Pore volume (cm^3/g)	2.60	2.62	4.38

The calculated crystallite size (summarized in Table 1) shows that GS-NMC has a slightly smaller crystallite size (approximately 18 nm) than SG-NMC (approximately 22 nm) and SS-NMC (approximately 19 nm), along with the lowest microstrain (4.28×10^{-3}) among the three samples. The refined lattice parameters for GS-NMC ($a \approx 2.861$ Å, $c \approx 14.19$ Å) are in close agreement with the ideal values for a well-ordered NMC111 structure[5].

In comparison, SG-NMC exhibits a slightly larger c-parameter (≈14.21 Å), and SS-NMC shows a marginally expanded a-parameter (≈2.882 Å). These subtle deviations are likely related to differences in Ni^{2+}/Li^{+} interlayer mixing. A higher degree of Ni^{2+} occupancy in Li^{+} sites typically cause contraction of the c-axis and expansion of the a–b lattice. The data, therefore, suggest that the green method achieved the lowest cation disorder, followed by the sol–gel method, with the solid-state sample likely having the highest Ni/Li mixing. All the synthesized samples exhibit diffraction patterns corresponding to a pristine phase layered oxide structure. The absence of impurity peaks in GS-NMC underscores the effectiveness of the kiwi extract in producing a pure product. In contrast, the Li_2CO_3 impurity observed in the solid-state sample is a common problem when lithium is lost or not fully homogenized.

The (003) peak positions (around 18.7° 2θ) also provide insight into the average Ni oxidation state. All three samples display (003) peaks at similar angles, which indicates a comparable average oxidation state for Ni. A higher Ni^{3+} content would shift the (003) peak to lower angles due to greater electrostatic repulsion in the Li layer. These results suggest that the bulk stoichiometry (and thus the Ni^{2+}/Ni^{3+} ratio required to charge-balance Mn^{4+} and Co^{3+}) is essentially the same across all samples, as expected from the use of identical nominal compositions. In summary, XRD confirms that the green-synthesized NMC is structurally comparable to (or even superior to) that of conventional methods. The green route produced a well-crystallized NMC without the need for prolonged high-temperature treatment. This is likely because the exothermic decomposition of the kiwi extract during calcination provided an instantaneous high local temperature, which promoted crystallization, while the short overall calcination time limited Li-volatilization.

The FTIR and Raman spectroscopy provide further evidence of differences in surface composition and lattice ordering. In the FTIR spectra (Figure 1b), SG-NMC and SS-NMC display distinct absorption bands at approximately 1420–1480 cm^{-1} and around 860 cm^{-1}, which are characteristic of carbonate species, most likely arising from surface-bound Li_2CO_3[31]. These bands are markedly weaker in GS-NMC, which is consistent with the XRD results, which show fewer carbonate impurities. Broad O–H stretching features (approximately 3400 cm^{-1}), attributed to adsorbed moisture or surface hydroxyls, appear in all samples. However, GS-NMC displays a slightly weaker O–H signature, which suggests reduced water adsorption potentially due to a more hydrophobic surface or lower surface LiOH content. The Raman spectra (Figure 1c) show two main bands at approximately 480 cm^{-1} (Eg mode) and 590 cm^{-1} (A1g mode), which are characteristic of layered NMC structures. Among the samples, GS-

NMC exhibits the sharpest Raman peaks and the highest A1g/Eg intensity ratio, which indicates improved layered ordering and minimal cation mixing. Cation disorder typically broadens and shifts these modes. In contrast, SS-NMC shows broader peaks and a noticeable shoulder at approximately 620 cm^{-1}, which suggests the presence of a spinel-like or disordered phase. These vibrational analyses further support the notion that the green-synthesized NMC possesses the most well-ordered structure and the fewest secondary phases, whereas the solid-state material exhibits greater structural disorder and a higher carbonate residue.

Morphology and Porosity

The electron microscopy images in Figure 2 illustrate clear morphological differences among the synthesized NMC samples. The sol–gel NMC (Figure 2a, d) consists of aggregates of plate-like particles with lateral dimensions of several hundred nanometers. In comparison, the solid-state NMC (Figure 2b, e) contains irregular, micron-scale agglomerates formed through extensive sintering and grain coalescence, which are typical of high-temperature solid-state reactions. In stark contrast, the green-synthesized NMC (Figure 2c, f) reveals a highly porous architecture composed of nanoscale primary particles (approximately 20–40 nm) assembled into a semi-porous, foam-like network. This nanostructured morphology is likely the result of rapid gas evolution during the combustion of kiwi extract organics, which inhibits particle fusion and promotes fine dispersion of the particles.

<Figure_2>

The quantitative analysis from SEM and TEM (Table 1) reveals average particle sizes of approximately 40 nm for SG-NMC, greater than 50 nm for SS-NMC, and around 30 nm for GS-NMC, which corroborates the visual observations. Consistently, BET measurements (Figure S2, Table 1) show that GS-NMC has the largest specific surface area (50–60 $m^2 \cdot g^{-1}$),

followed by SG-NMC (approximately 30 $m^2 \cdot g^{-1}$) and SS-NMC (approximately 20 $m^2 \cdot g^{-1}$). The increased surface area and nanostructured texture of GS-NMC are expected to enhance electrolyte accessibility and interfacial charge-transfer kinetics in aqueous electrochemical systems.

Each NMC sample displays a type IV nitrogen adsorption isotherm with a hysteresis loop, which indicates mesoporous characteristics. The pore size distribution (determined via BJH analysis) for GS-NMC centers around 8–12 nm (mesopores between primary particles). In contrast, SG-NMC and SS-NMC exhibit broader pore distributions, with some larger voids (greater than 20 nm), particularly in SS-NMC, due to inter-agglomerate gaps. The significantly enhanced porosity of GS-NMC can be attributed to the gas-releasing decomposition of organic components from the kiwi extract, which effectively creates micro- and mesopores.

The hierarchical porosity is highly beneficial for a battery electrode: it increases the electrolyte contact area and facilitates Li^+ transport to active sites. The qualitative radar chart (Figure S3 in the Supporting Information) illustrates this point: GS-NMC scores highest in "Electrolyte Penetration" and "Structural Stability" among the three synthesis routes. This result aligns with the expectation that the porous architecture and robust lattice of GS-NMC should lead to enhanced electrochemical utilization. From the green synthesis perspective, it is noteworthy that the use of a natural extract provides not only environmental benefits but also tangible material advantages such as higher surface area and smaller, more uniform particles. These characteristics are often difficult to achieve via traditional methods without additional grinding or templating steps.

Composition and Surface Chemistry

The TEM analysis (Figure 3) enables further insight into the crystallite morphology and

confirms the phase purity at the nanoscale. Specifically, high-resolution TEM images of GS-NMC revealed clear lattice fringes with a d-spacing of approximately 0.47 nm, which corresponds to the (003) planes of the layered structure. Selected-area electron diffraction (SAED) patterns show well-defined rings that match the NMC lattice spacings and indicate a polycrystalline yet highly ordered nature. Similarly, the SAED patterns for SG-NMC and SS-NMC confirm the layered structure, though SS-NMC's pattern shows slightly diffuse rings consistent with its greater lattice strain/defects. Energy dispersive X-ray (EDX) mapping in TEM/SEM (Figure S4) demonstrates a uniform distribution of Ni, Mn, and Co in all samples, with no significant compositional segregation — an expected result given the identical target stoichiometry and thorough mixing in all synthesis routes. The atomic ratios measured using EDX (Figure S5) were close to 1:1:1 (Ni:Mn:Co), with an accuracy of ±5% for each sample. These results confirm that the green extract does not introduce any deviation in metal stoichiometry. Trace elements from the kiwi extract (such as K, Ca, or others commonly found in plant matter) were below the EDX detection limits, which suggests they were either not incorporated or removed during the washing process.

<Figure_3>

The XPS was used to investigate the surface chemical environment of the synthesized NMC powders, probing the outermost layer approximately 5 nm thick. The wide-scan spectra (Figures 4, S6) confirm the presence of Ni, Mn, Co, O, C, and trace Li signals in all samples. Furthermore, high-resolution Ni 2p spectra (Figure 4a,d,g) reveal features typical of a mixed-valence Ni^{2+}/Ni^{3+} system—with the Ni $2p_{3/2}$ main peaks located at approximately 855–856 eV and satellite peaks near 861–863 eV. Deconvolution reveals that GS-NMC had a slightly higher surface Ni^{3+} fraction (approximately 50%) than SG-NMC (approximately 45%) and SS-NMC

(approximately 40%). In addition, because Ni^{3+} is associated with better electrochemical activity and lower cation mixing, this higher fraction in GS-NMC suggests a better surface configuration with fewer Ni^{2+} ions occupying lithium sites.

<Figure_4>

Furthermore, the Co $2p_{3/2}$ peaks (Figure 4b,e,h) centered around 779–781 eV confirm that cobalt existed predominantly in the Co^{3+} oxidation state across all samples, with no clear indication of Co^{2+}. Similarly, the Mn $2p_{3/2}$ peaks (Figure 4c,f,i) at approximately 642 eV indicate that Mn^{4+} was the dominant species because no fitting component near 641 eV (indicative of Mn^{3+}) was necessary. This oxidation-state distribution supports the intended NMC111 composition, with surface transition metals present primarily as Ni^{2+}/Ni^{3+}, Co^{3+}, and Mn^{4+}.

A more distinct difference appears in the O 1s and C 1s regions. The O 1s spectra (Figure S6a,d,g) for GS-NMC display a strong lattice oxide peak at approximately 529.6 eV and a weak shoulder at approximately 531–532 eV, which corresponds to surface hydroxide or carbonate species. In contrast, SS-NMC exhibits a more prominent high-binding-energy shoulder (approximately 531.5 eV), along with a strong C 1s peak (Figure S6b,e,h) at approximately 289.5 eV—which is indicative of surface $–CO_3$ groups (e.g., Li_2CO_3). SG-NMC showed intermediate levels of these signals. Moreover, a quantitative comparison of carbonate-related C 1s intensity reveals the highest surface carbonate content in SS-NMC, followed by SG-NMC, and the lowest value in GS-NMC.

This trend matches the FTIR data and is consistent with residual lithium species (e.g., LiOH or Li_2O) reacting with atmospheric CO_2 during storage. The lower surface carbonate content and cleaner O 1s signal in GS-NMC further support its enhanced surface stability and superior

structural purity[32]. The lower amount of surface carbonate on GS-NMC suggests either a reduced residual Li (due to optimal calcination and possibly slight self-passivation by carbon from the extract) or a different surface termination that is less prone to carbonation. The practical implication of reduced surface Li_2CO_3 is significant. Li_2CO_3 is known to consume electrolytes and evolve CO_2 gas in full cells, and it can trigger the release of lattice oxygen at high voltages, which exacerbates electrolyte degradation[32]. Therefore, the greener synthesis seems to impart a "cleaner" surface, which could improve electrode–electrolyte interface stability. In addition, any carbon residual from the organic fuel (e.g., a thin amorphous carbon layer) could not be distinctly observed in XPS apart from the adventitious carbon signal. However, if present in trace amounts, it may enhance electronic conductivity locally. No obvious graphitic carbon was detected (no sharp peak at approximately 284.0 eV beyond baseline carbon), which indicates that the kiwi extract combustion did not leave a significant conductive carbon coating—which is expected given the complete calcination in air. The surface analysis confirms that GS-NMC contains the least amount of undesirable surface species (like Li_2CO_3) and that all three methods yield the correct transition-metal oxidation states. The differences in Ni^{3+} fraction suggest slightly better electrochemical activation for the green sample; however, since all samples have similar bulk stoichiometry, the primary distinctions lie in morphology and purity rather than gross composition.

Electrochemical behavior in aqueous 1 M LiOH

In order to evaluate the electrochemical properties resulting from these structural differences, we investigated the samples in a 1 M LiOH three-electrode cell. Although this aqueous system cannot replicate the full voltage range of a lithium-ion cell, it allows us to examine surface redox reactions (primarily Ni-based) as well as the charge-transfer processes. Cyclic

voltammetry at various scan rates and repeated cycling at a fixed scan rate were performed for each sample, as shown in Figure 5

<Figure_5>

In the initial cyclic voltammograms (CVs) of the first cycle, all samples exhibited a pair of redox peaks, which suggests a reversible surface redox couple. For example, GS-NMC showed a prominent anodic peak around -0.01 V versus Ag/AgCl and a corresponding cathodic peak near -0.29 V. These peaks can be attributed to the Ni(II)/Ni(III) oxidation and subsequent reduction (likely the formation/removal of a NiOOH-like surface layer). SG-NMC and SS-NMC show similar peaks but with notable differences in sharpness and separation. The GS-NMC peaks are the most symmetric and show the smallest peak potential separation (ΔEp), which suggests faster kinetics. SS-NMC displayed slightly broader peaks, with an anodic peak at −0.02 V and a cathodic peak at −0.31 V ($\Delta E_p \approx 0.29$ V), which is marginally larger than that of GS-NMC. This subtle increase in peak separation indicates slightly higher polarization and slower charge-transfer kinetics, likely due to the larger particle size and higher surface resistance of SS-NMC.

The electrochemical stability of the samples was evaluated through repeated CV cycling up to 100 cycles at a moderate scan rate (50 $mV \cdot s^{-1}$). Among the three, GS-NMC showed the most stable behavior, as it maintained nearly constant peak current densities and minimal shifts in redox-peak positions over the entire cycling duration. In comparison, SG-NMC showed a moderate decline in performance, with anodic and cathodic peak currents decreasing by approximately 10–15% and a slight increase in the peak separation (ΔE_p). The SS-NMC underwent the strongest degradation, with the current response dropping by approximately 20% and the peak positions shifting by approximately 50 mV after 100 cycles. These results suggest

that the green-synthesized NMC possesses a more electrochemically stable surface under alkaline aqueous conditions—potentially due to its higher surface integrity and reduced content of reactive surface species such as Li_2CO_3. In contrast, the performance drop in SS-NMC may result from microstructural damage, surface passivation, or dissolution of labile surface compounds into the electrolyte.

Further insight was gained from scan rate-dependent CVs collected between 10 and 50 $mV \cdot s^{-1}$. GS-NMC maintained sharp, quasi-rectangular current profiles even at higher scan rates, which indicates fast surface redox kinetics with minimal resistive distortion. SG-NMC also maintained discernible redox peaks, though with more pronounced broadening. Conversely, SS-NMC lost peak definition rapidly as the scan rate increased, with the voltammograms becoming increasingly resistive. The relationship between anodic peak current (i_{peak}) and the square root of the scan rate ($\nu^{1/2}$) is shown for all samples to evaluate the kinetic regime. GS-NMC exhibits the highest linearity ($R^2 \approx 0.99$), which is consistent with diffusion-controlled behavior despite the thin-film configuration, while SS-NMC deviated significantly from linearity—likely due to slower lithium-ion transport across larger or less accessible particles. These observations confirm that the green synthesis route not only provides structural and surface benefits but also translates into superior electrochemical reversibility and redox kinetics in aqueous conditions.

The Electrochemical impedance spectroscopy measurements provide quantitative support for the CV observations. Figure 6 (Nyquist plots) compares the impedance of the three electrodes at open-circuit potential (OCP). All spectra exhibit a high-frequency intercept corresponding to the solution resistance R_s, which is approximately 6.5 Ω, and similar for all samples, as expected in the same electrolyte. A depressed semicircle appears in the mid-

frequency region, which corresponds to the charge-transfer resistance (R_{ct}) coupled with double-layer capacitance. The latter is modeled as a constant phase element due to non-ideal capacitive behavior. The diameter of this semicircle is smallest for GS-NMC, intermediate for SG-NMC, and largest for SS-NMC. The electrochemical impedance spectra, when fitted with an equivalent circuit model revealed Rct values of approximately 320 Ω for GS-NMC, 540 Ω for SG-NMC, and 810 Ω for SS-NMC (±10 Ω). The GS-NMC electrode's R_{ct} is nearly half that of the solid-state one, which indicates a substantially faster charge-transfer process at the interface.

<Figure_6>

This result can be attributed to the higher surface area and possibly better electronic percolation of GS-NMC. Each primary particle is small and well-connected to conductive carbon, with a possible presence of surface carbon from the organic synthesis route. In addition, the absence of blocking surface films (such as Li_2CO_3), which can impede charge transfer in SG and SS-NMC, further contributes to the improved performance. The low-frequency tail of the Nyquist plot (Warburg line) also shows a steeper slope for GS-NMC, which is consistent with shorter diffusion lengths for Li^+ (or OH^-) within the material. Overall, the EIS results confirm that the green-synthesized NMC offers superior electrochemical interface properties—a promising indication for high-rate performance in practical battery applications.

Figure 7 shows the galvanostatic profiles and long-term cycling behavior of the three NMC samples in the aqueous 1 M LiOH electrolyte. At the lowest current density (0.1 A/g), the green-synthesized NMC (Figure 7c)) exhibits the highest specific discharge capacity (approximately 125 $mAh \cdot g^{-1}$), outperforming both sol–gel (SG-NMC, approximately 110 $mAh \cdot g^{-1}$) and solid-state NMC (SS-NMC). The voltage profile of GS-NMC, with a charge

plateau at approximately +0.25 V and a discharge plateau at approximately +0.15 V, indicates a well-defined redox process and minimal polarization. By contrast, SG-NMC and especially SS-NMC display more sloped voltage profiles and larger hysteresis (Figure 7a,b). For example, SS-NMC shows a charge endpoint near +0.40 V and a discharge endpoint near 0 V, which indicates higher internal resistance and possible side reactions.

<Figure_7>

As the current density increases to 1 A/g, all samples exhibit the expected drops in capacity and increased polarization. Notably, GS-NMC retains approximately 80 $mAh \cdot g^{-1}$ at 1 A/g, while SG-NMC and SS-NMC drop to approximately 60 $mAh \cdot g^{-1}$ and 50 $mAh \cdot g^{-1}$, respectively. SS-NMC reaches the upper cutoff voltage more quickly during charging, which is consistent with a higher charge-transfer resistance (R_{ct}) and limited surface utilization. These observations align well with earlier CV and EIS results, which also suggest a superior rate capability and lower impedance in GS-NMC.

Moreover, the long-term cycling performance at 0.5 A/g (Figure 7d-f)) highlights the structural and electrochemical stability of each sample. SG-NMC begins at approximately 85 $mAh \cdot g^{-1}$ and retains about 60 $mAh \cdot g^{-1}$ after 1000 cycles (70% retention), with its Coulombic efficiency stabilizing at approximately 98–100% after an initial period of 90% efficiency—likely due to early-stage side reactions. SS-NMC starts at about 75 $mAh \cdot g^{-1}$ but decreases to approximately 50 $mAh \cdot g^{-1}$ (67% retention), and its efficiency remains slightly lower (99%). This behavior suggests ongoing parasitic processes, such as the slow dissolution of Li_2CO_3 or the leaching of transition metals into the electrolyte.

In stark contrast, GS-NMC demonstrates both high capacity and excellent retention. Its initial capacity (approximately 120 $mAh \cdot g^{-1}$) decreases only slightly to approximately 110 $mAh \cdot g^{-1}$

after 1000 cycles, which corresponds to approximately 92% retention. Furthermore, its Coulombic efficiency reaches 99–100% within the first 10 cycles and remains stable thereafter. The stability and high reversibility reflect the structural robustness and chemically clean surface of GS-NMC, which highlights the advantages of the green synthesis route for aqueous electrochemical systems.

The superior stability of GS-NMC in this aqueous testing regime highlights its robust structural and interfacial nature. However, despite the aggressive conditions (aqueous electrolyte, repeated Ni redox cycling, and potential for CO_2 absorption), the GS-NMC electrode exhibits minimal performance loss, which implies that it resists common degradation mechanisms such as transition metal dissolution or mechanical disintegration. This finding can be attributed to its strong structural integrity (thanks to low microstrain and a stable layered framework) and likely a self-passivating surface that prevents continuous reaction with the electrolyte.

Moreover, SG-NMC's moderate fading could be due to some structural rearrangements or minor dissolution (citric-derived synthesis often yields slightly less structurally dense materials than co-precipitation). Moreover, the larger capacity fade of SS-NMC is consistent with its higher level of surface impurities and defects that contribute to performance loss. For example, residual Li_2CO_3 may gradually react, or micro-cracks in larger particles may cause a loss of electrical contact. Importantly, although the absolute capacities here are specific to the aqueous system, the observed trends are indicative of real battery behavior. A material that exhibits a higher pseudocapacitive charge and greater stability is likely to possess a higher active surface area and a more stable lattice, which would also support lithium intercalation in a full cell without rapid capacity loss. The GS-NMC's ability to maintain nearly 100% Coulombic efficiency means it undergoes purely reversible redox transitions with no build-up of

irreversible changes a promising sign of a long cycle life. In addition, the differences in Coulombic efficiency early in cycling (SG had approximately 90% initially, SS approximately 85%, GS approximately 95%) may be related to the reduction of surface species, such as pre-existing Ni^{3+} or surface oxygen species, which occur during the initial cycles or minor electrolyte decomposition. The higher initial efficiency of GS-NMC suggests that fewer parasitic surface species are presented initially, which again reflects a cleaner surface.

Post-Cycling Structural Analysis

To further confirm the advantages of the green synthesis, ex-situ XRD and SEM analyses were conducted on electrodes after 1000 cycles, following electrolyte removal and rinsing. As shown in Figure 8a, the XRD patterns of the GS-NMC electrode retained all characteristic peaks of the layered oxide without the emergence of secondary phases. In contrast, both SG-NMC and SS-NMC exhibit signs of surface carbonation. Notably, the post-cycling XRD patterns of SS-NMC show distinct peaks that correspond to Li_2CO_3 (marked with #), which suggests substantial formation or crystallization of Li_2CO_3 during cycling, likely caused by lithium leaching and subsequent reaction with ambient CO_2. SG-NMC shows only very faint traces of such peaks, while GS-NMC shows none, which is consistent with its stable cycling behavior. The lattice parameters of GS-NMC after cycling remained virtually unchanged (within experimental error), indicating excellent structural stability.

<Figure_8>

In contrast, SS-NMC's *c*-parameter shows a slight reduction possibly due to mild lattice collapse from cumulative Ni-oxidation or proton insertion (protons from water can exchange with Li^+ in near-surface sites over prolonged cycling, which tends to shrink the lattice). The SEM images (Figure 8b-g) of the cycled samples tell a similar story: GS-NMC (Figure 8f, g)

preserves its porous nanostructure with only minor agglomeration; the particles largely retain their size, and no severe cracking or exfoliation is observed.

SG-NMC (Figure 8b,c) shows some particle coalescence and surface smoothing, perhaps due to slight dissolution and re-deposition of metal (forming "glue" between particles). SS-NMC (Figures 8d,e) exhibits the largest change – its initially dense particles have developed noticeable microcracks and some surface deposits, likely a mixture of $LiOH/Li_2CO_3$ or $Ni(OH)_2$ that precipitated out. These physical degradations in SS-NMC correlate with its performance drop, as loss of particle integrity can disrupt electrical pathways and expose fresh surfaces to side reactions.

Overall, the post-mortem analyses reinforce that the green-synthesized NMC possesses superior structural resilience in an aqueous environment. Even after an extreme 1000-cycle test, GS-NMC remains phase-pure and morphologically intact, whereas conventional sol–gel and solid-state NMC undergo the formation of inactive phases and structural damage. These results suggest that GS-NMC could also better withstand the rigorous volume changes and surface reactions that occur in practical battery cells.

Implications for battery applications

While our electrochemical measurements were performed in a three-electrode aqueous cell (primarily to isolate and compare the intrinsic material properties), the observed trends are highly relevant to the actual performance of lithium-ion batteries. The combination of high surface area and stable structure in GS-NMC is expected to translate into improved rate capability and cycle life in a full cell. A higher surface area typically results in greater electrode–electrolyte contact and shorter Li^+ diffusion distances, which can enhance rate performance, but only if the surface is also engineered to minimize side reactions. The green

synthesis method achieves this balance by producing a finely divided morphology without introducing problematic surface residues. The lower charge-transfer resistance measured for GS-NMC further implies that, in a battery, it would exhibit lower polarization under load and deliver higher usable capacity at high C-rates.

Additionally, the reduced Ni/Li disorder points to a potentially higher initial capacity (because every Ni in the Li layer represents an electrochemically inactive defect). Even though full cells were not assembled in this study, GS-NMC is expected to exhibit slightly improved first-cycle efficiency and capacity due to its cleaner surface. A lower Li_2CO_3 content would reduce the initial irreversible consumption of Li^+ required to form SEI components in a nonaqueous cell.

It is also important to note the environmental and economic advantages of the green synthesis route. This method eliminates the need for synthetic organic additives, such as costly alkoxides or templating agents, and utilizes renewable biomass. Moreover, the success of kiwi extract in producing a high-performance NMC opens the door for exploring other natural extracts (such as tea, aloe vera, etc.) as both fuel and functional additives in cathode synthesis[17]. Given that large-scale battery manufacturing is seeking ways to reduce its carbon footprint, such approaches could become feasible if they also confer performance benefits, as demonstrated in this case. Future work should include scaling up the green synthesis and testing of GS-NMC in real lithium-ion cells (with organic electrolytes) to confirm the benefits in realistic settings. Parameters such as rate capability at high C (e.g., 5C, 10C) and long-term cycle life at high voltage (up to 4.3 V vs. Li^+/Li) will be the ultimate test. However, the aqueous screening performed in this study serves as a valuable interim step, as it rapidly identified the GS-NMC as the top candidate among the three synthesis methods and helps to guide the focus of subsequent full-cell tests.

In summary, the green-synthesized $LiNi_{1/3}Mn_{1/3}Co_{1/3}O_2$ exhibits excellent structural integrity, minimal cation mixing, enhanced surface area, and reduced charge-transfer resistance, all key attributes for high-performance lithium-ion battery cathodes. Despite the constraints of the aqueous electrolyte system, these features result in superior reversible pseudocapacity and long-term stability. These findings suggest that, under conventional non-aqueous LIB conditions, GS-NMC is likely to exhibit even greater kinetic performance and durability. This work highlights the potential of bio-assisted synthesis methods to provide both environmental sustainability and electrochemical excellence in next-generation battery materials.

Conclusion

A comprehensive comparative study was conducted on $LiNi_{1/3}Mn_{1/3}Co_{1/3}O_2$ (NMC) cathodes synthesized using green (kiwi extract-assisted), sol–gel, and solid-state methods. The green synthesis route produced NMC with superior structural and surface characteristics, including a phase-pure layered structure, minimal Li/Ni cation disorder, high crystallinity, and a porous nanoscale morphology, which resulted in an increased surface area. While the sol–gel method also produced well-ordered NMC, it exhibited slightly higher levels of residual lithium species and lower porosity. The solid-state method, although synthetically straightforward, yielded larger particles with the most pronounced impurities. Electrochemical performance was evaluated in a 1 M LiOH aqueous three-electrode system, which served as an accelerated-screening platform. The green-synthesized NMC (GS-NMC) exhibited the highest accessible reversible capacity, the lowest charge-transfer resistance (R_{ct}), and excellent cycling stability, retaining approximately 92% of its initial capacity after 1000 cycles. In contrast, both the sol–gel and solid-state samples exhibited greater capacity fading. Post-cycling structural analysis

confirmed the excellent stability of GS-NMC, with no secondary phase formation, whereas the other samples showed accumulation of Li_2CO_3 and evidence of microstructural degradation. These findings underscore that, beyond its environmental benefits, green synthesis provides intrinsic material advantages, producing cathodes with robust structural stability and enhanced electrochemical performance. This makes it a compelling strategy for next-generation battery materials.

It is essential to acknowledge the limitations of the aqueous testing approach: it does not fully probe the lithiation capacity or the high-voltage behavior of NMC. Nevertheless, the method is effective for gauging relative performance metrics such as charge transfer resistance and cyclability related to surface processes. The exemplary performance of the green-synthesized NMCs in this study strongly indicates their potential for application in real-life lithium-ion batteries. By utilizing natural extracts in material synthesis, this work demonstrates a pathway to simultaneously address environmental sustainability and enhance material quality. Future studies will focus on integrating GS-NMC into full cells and evaluating key metrics, such as rate performance above 1C and cycle life over hundreds of deep lithiation and delithiation cycles. In addition, exploring the chemistry of the kiwi may provide insights into which components (such as polyphenols or sugars) contribute most significantly to the improved outcomes, potentially guiding the refinement of green synthesis protocols.

In conclusion, the green synthesis approach mediated by kiwi extract offers a simple and eco-friendly pathway for producing $LiNi_{1/3}Mn_{1/3}Co_{1/3}O_2$ cathode materials. The resulting NMC exhibits improved structural coherence, reduced cation disorder, increased surface area, and lower charge-transfer resistance—all of which are confirmed through aqueous-phase electrochemical assessments. These characteristics suggest strong potential for application in

next-generation lithium-ion batteries. More broadly, this work demonstrates that natural extract-based synthesis can provide not only environmental advantages but also tangible performance benefits, thereby bridging the gap between green chemistry and advanced energy storage technologies.

Acknowledgements

This research was supported by the Global Research Development Center (GRDC) Cooperative Hub Program through the National Research Foundation of Korea (NRF) funded by the Ministry of Science and ICT (MSIT) (RS-2023-00257595). This work was supported by the National Research Foundation of Korea (NRF) grant funded by the Korea government (MSIT) (No. RS-2024-00413272).

References

1. Jung, R.; Metzger, M.; Maglia, F.; Stinner, C.; Gasteiger, H. A., Oxygen release and its effect on the cycling stability of LiNixMnyCozO_2 (NMC) cathode materials for Li-ion batteries. *Journal of The Electrochemical Society* **2017,** *164* (7), A1361.
2. Garcia, J. C.; Bareño, J.; Yan, J.; Chen, G.; Hauser, A.; Croy, J. R.; Iddir, H., Surface structure, morphology, and stability of Li ($Ni_{1/3}Mn_{1/3}Co_{1/3}$)O_2 cathode material. *The Journal of Physical Chemistry C* **2017,** *121* (15), 8290-8299.
3. Yin, L.; Tatara, R.; Nakamoto, K.; Yamazaki, S.; Takaishi, R.; Shiiyama, E.; Matsuyama, T.; Komaba, S., Electrochemical Properties of Powdery Li $Ni_{1/3}Mn_{1/3}Co_{1/3}O_2$ Electrodes with Styrene-Acrylic-Rubber-Based Latex Binders at High Voltage. *ACS Applied Materials & Interfaces* **2024,** *16* (49), 67577-67586.
4. Belharouak, I.; Sun, Y.-K.; Liu, J.; Amine, K., Li ($Ni_{1/3}Mn_{1/3}Co_{1/3}$)O_2 as a suitable cathode for high power applications. *Journal of power sources* **2003,** *123* (2), 247-252.
5. Chen, Z.; Wang, J.; Chao, D.; Baikie, T.; Bai, L.; Chen, S.; Zhao, Y.; Sum, T. C.; Lin, J.; Shen, Z., Hierarchical porous $LiNi_{1/3}Mn_{1/3}Co_{1/3}O_2$ nano-/micro spherical cathode material: minimized cation mixing and improved Li+ mobility for enhanced electrochemical performance. *Scientific reports* **2016,** *6* (1), 25771.
6. Teichert, P.; Eshetu, G. G.; Jahnke, H.; Figgemeier, E., Degradation and aging routes of Ni-rich cathode based Li-ion batteries. *Batteries* **2020,** *6* (1), 8.
7. Liu, W.; Oh, P.; Liu, X.; Lee, M. J.; Cho, W.; Chae, S.; Kim, Y.; Cho, J., Nickel-rich layered lithium transition-metal oxide for high-energy lithium-ion batteries. *Angewandte Chemie International Edition* **2015,** *54* (15), 4440-4457.
8. Saaid, F. I.; Kasim, M. F.; Winie, T.; Elong, K. A.; Azahidi, A.; Basri, N. D.; Yaakob, M. K.; Mastuli, M. S.; Shaffee, S. N. A.; Zolkiffly, M. Z., Ni-rich lithium nickel manganese cobalt oxide cathode materials: A review on the synthesis methods and their electrochemical performances. *Heliyon* **2024,** *10* (1).
9. Malik, M.; Chan, K. H.; Azimi, G., Review on the synthesis of $LiNi_xMn_yCo_{1-x-y}O_2$ (NMC) cathodes for lithium-ion batteries. *Materials Today Energy* **2022,** *28*, 101066.
10. Cao, X.; Zhao, Y.; Zhu, L.; Xie, L.; Cao, X.; Xiong, S.; Wang, C., Synthesis and characterization of Li $Ni_{1/3}Mn_{1/3}Co_{1/3}O_2$ as cathode materials for Li-ion batteries via an efficacious sol-gel method. *International Journal of Electrochemical Science* **2016,** *11* (6), 5267-5278.
11. Cho, T.; Park, S.; Yoshio, M.; Hirai, T.; Hideshima, Y., Effect of synthesis condition on the structural and electrochemical properties of Li($Ni_{1/3}Mn_{1/3}Co_{1/3}$)O_2 prepared by carbonate co-precipitation method. *Journal*

of power sources **2005,** *142* (1-2), 306-312.
12. Wang, L.; Huang, B.; Xiong, W.; Tong, M. e.; Li, H.; Xiao, S.; Chen, Q.; Li, Y.; Yang, J., Improved solid-state synthesis and electrochemical properties of $LiNi_{0.6}Mn_{0.2}Co_{0.2}O_2$ cathode materials for lithium-ion batteries. *Journal of Alloys and Compounds* **2020,** *844*, 156034.
13. Yue, P.; Wang, Z.; Peng, W.; Li, L.; Guo, H.; Li, X.; Hu, Q.; Zhang, Y., Preparation and electrochemical properties of submicron LiNi0. 6Co0. 2Mn0. 2O2 as cathode material for lithium ion batteries. *Scripta materialia* **2011,** *65* (12), 1077-1080.
14. Danks, A. E.; Hall, S. R.; Schnepp, Z., The evolution of 'sol–gel'chemistry as a technique for materials synthesis. *Materials Horizons* **2016,** *3* (2), 91-112.
15. Liu, H.; Wu, Y.; Rahm, E.; Holze, R.; Wu, H., Cathode materials for lithium ion batteries prepared by sol-gel methods. *Journal of Solid State Electrochemistry* **2004,** *8*, 450-466.
16. Kızıltaş-Yavuz, N.; Herklotz, M.; Hashem, A. M.; Abuzeid, H. M.; Schwarz, B.; Ehrenberg, H.; Mauger, A.; Julien, C. M., Synthesis, structural, magnetic and electrochemical properties of $Li\ Ni_{1/3}Mn_{1/3}Co_{1/3}O_2$ prepared by a sol–gel method using table sugar as chelating agent. *Electrochimica Acta* **2013,** *113*, 313-321.
17. Li, J.; Li, Y.; Wu, H.; Naraginti, S.; Wu, Y., Facile synthesis of ZnO nanoparticles by Actinidia deliciosa fruit peel extract: Bactericidal, anticancer and detoxification properties. *Environmental Research* **2021,** *200*, 111433.
18. Villagrán, Z.; Anaya-Esparza, L. M.; Velázquez-Carriles, C. A.; Silva-Jara, J. M.; Ruvalcaba-Gómez, J. M.; Aurora-Vigo, E. F.; Rodríguez-Lafitte, E.; Rodríguez-Barajas, N.; Balderas-León, I.; Martínez-Esquivias, F., Plant-based extracts as reducing, capping, and stabilizing agents for the green synthesis of inorganic nanoparticles. *Resources* **2024,** *13* (6), 70.
19. Singh, H.; Desimone, M. F.; Pandya, S.; Jasani, S.; George, N.; Adnan, M.; Aldarhami, A.; Bazaid, A. S.; Alderhami, S. A., Revisiting the green synthesis of nanoparticles: uncovering influences of plant extracts as reducing agents for enhanced synthesis efficiency and its biomedical applications. *International journal of nanomedicine* **2023**, 4727-4750.
20. Abuzeid, H. M.; Julien, C. M.; Zhu, L.; Hashem, A. M., Green synthesis of nanoparticles and their energy storage, environmental, and biomedical applications. *Crystals* **2023,** *13* (11), 1576.
21. NISHIYAMA, I.; Fukuda, T.; Shimohashi, A.; Oota, T., Sugar and organic acid composition in the fruit juice of different Actinidia varieties. *Food science and technology research* **2008,** *14* (1), 67-73.
22. Bursal, E.; Gülçin, İ., Polyphenol contents and in vitro antioxidant activities of lyophilised aqueous extract of kiwifruit (Actinidia deliciosa). *Food research international* **2011,** *44* (5), 1482-1489.
23. Kodasi, B.; Kamble, R. R.; Manjanna, J.; Hoolageri, S. R.; Bheemayya, L.; Nadoni, V. B.; Bayannavar, P. K.; Dixit, S.; Vootla, S. K.; Kumbar, V. M., Adept green synthesis of Cu_2O nanoparticles using Kiwi fruit (Actinidia deliciosa) juice and Studies on their cytotoxic activity and antimicrobial evaluation. *Journal of Trace Elements and Minerals* **2023,** *3*, 100044.
24. Ahn, H.; Kim, D.; Lee,M.;Nam, K. W.,Challenges and possibilities for aqueous battery systems. *Communications Materials* **2023,** *4* (1), 37.
25. Chen, S.; Zhang, M.; Zou, P.; Sun, B.; Tao, S., Historical development and novel concepts on electrolytes for aqueous rechargeable batteries. *Energy & Environmental Science* **2022,** *15* (5), 1805-1839.
26. Suo, L.; Borodin, O.; Gao, T.; Olguin, M.; Ho, J.; Fan, X.; Luo, C.; Wang, C.; Xu, K., "Water-in-salt" electrolyte enables high-voltage aqueous lithium-ion chemistries. *Science* **2015,** *350* (6263), 938-943.
27. Hong, S.; Choi, Z.; Hwang, B.; Matic, A., Research Trends and Future Perspectives on Zn-Ion Batteries Using Ga-Based Liquid Metal Coatings on Zn Anodes. *ACS Energy Letters* **2024,** *9* (11), 5421-5433.
28. von Wald Cresce, A.; Xu, K., Aqueous lithium-ion batteries. *Carbon Energy* **2021,** *3* (5), 721-751.
29. Wang, Y.; Yi, J.; Xia, Y., Recent progress in aqueous lithium-ion batteries. *Advanced Energy Materials* **2012,** *2* (7), 830-840.
30. Luo, J.-Y.; Cui, W.-J.; He, P.; Xia, Y.-Y., Raising the cycling stability of aqueous lithium-ion batteries by eliminating oxygen in the electrolyte. *Nature chemistry* **2010,** *2* (9), 760-765.
31. Buijs, K.; Schutte, C., The infra-red spectra and structures of Li_2CO_3 and anhydrous Na_3CO_3. *Spectrochimica Acta* **1961,** *17* (9-10), 927-932.
32. Kaufman, L. A.; McCloskey, B. D., Surface lithium carbonate influences electrolyte degradation via reactive oxygen attack in lithium-excess cathode materials. *Chemistry of Materials* **2021,** *33* (11), 4170-4176.

Figure

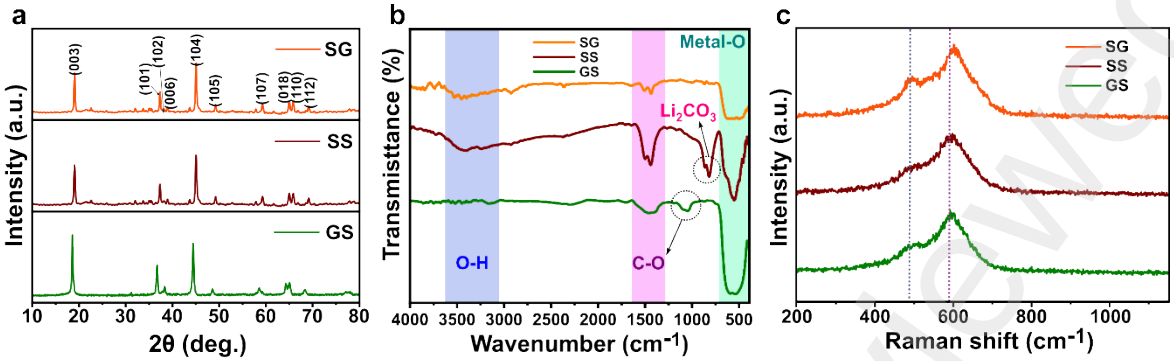

Figure 1. (a) XRD patterns, (b) FT-IR spectra, and (c) Raman spectra of NMC cathodes prepared using sol–gel (SG), solid-state (SS), and green synthesis (GS) methods.

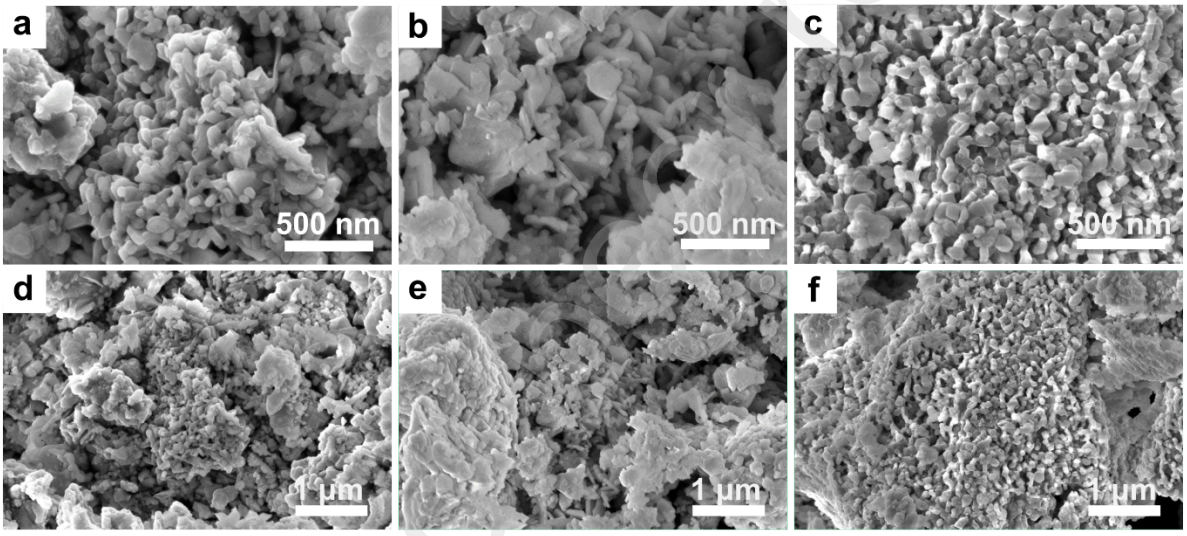

Figure 2. SEM images of NMC cathode materials synthesized using the sol–gel (a, d), solid-state (b, e), and green (c, f) methods. Top row: high-magnification images; bottom row: low-magnification images.

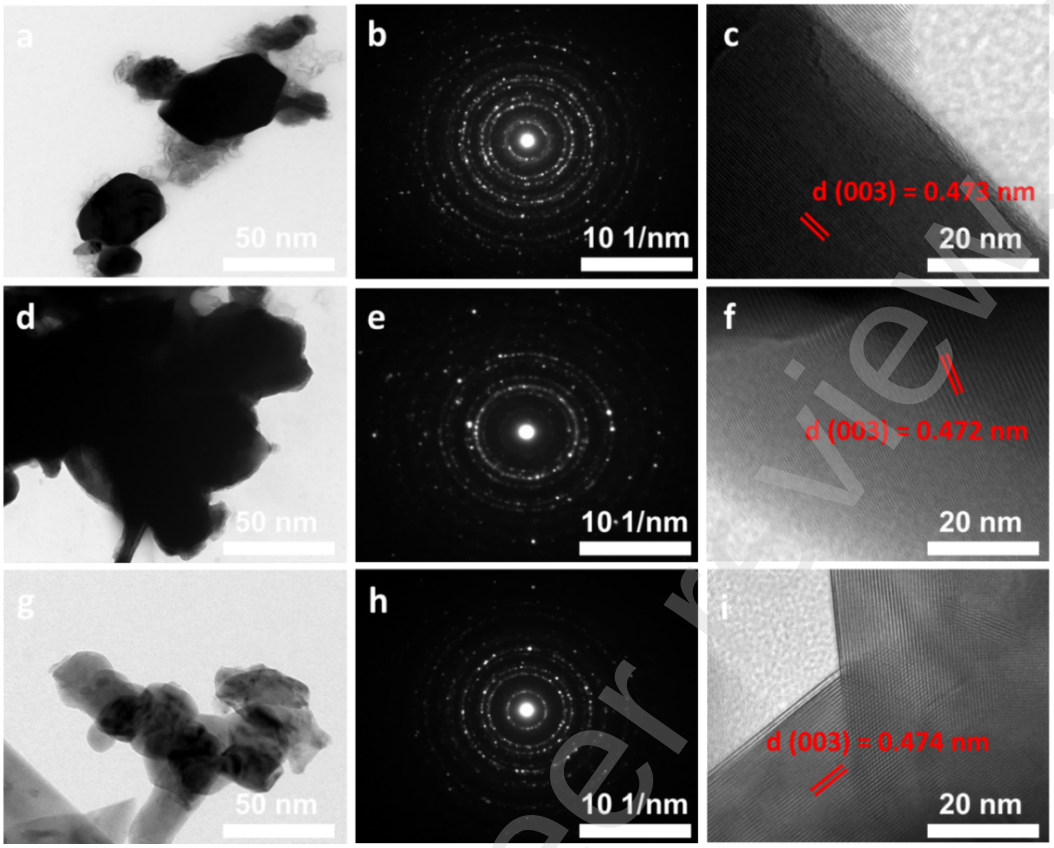

Figure 3. TEM images of NMC synthesized via the (a–c) sol–gel (SG), (d–f) solid-state (SS), and (g–i) green synthesis (GS) methods.

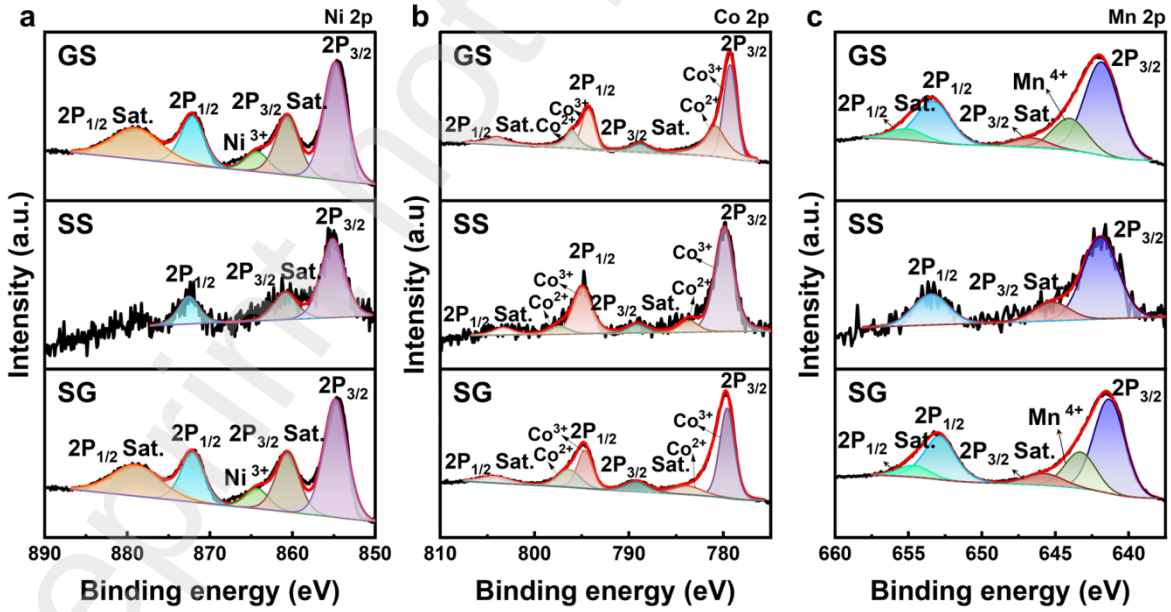

Figure 4. High-resolution XPS spectra of Ni 2p (a), Co 2p (b), and Mn 2p (c) for NMC samples synthesized using sol–gel (SG), solid-state (SS), and green synthesis (GS) methods. The spectra are arranged from bottom to top in the order SG, SS, GS.

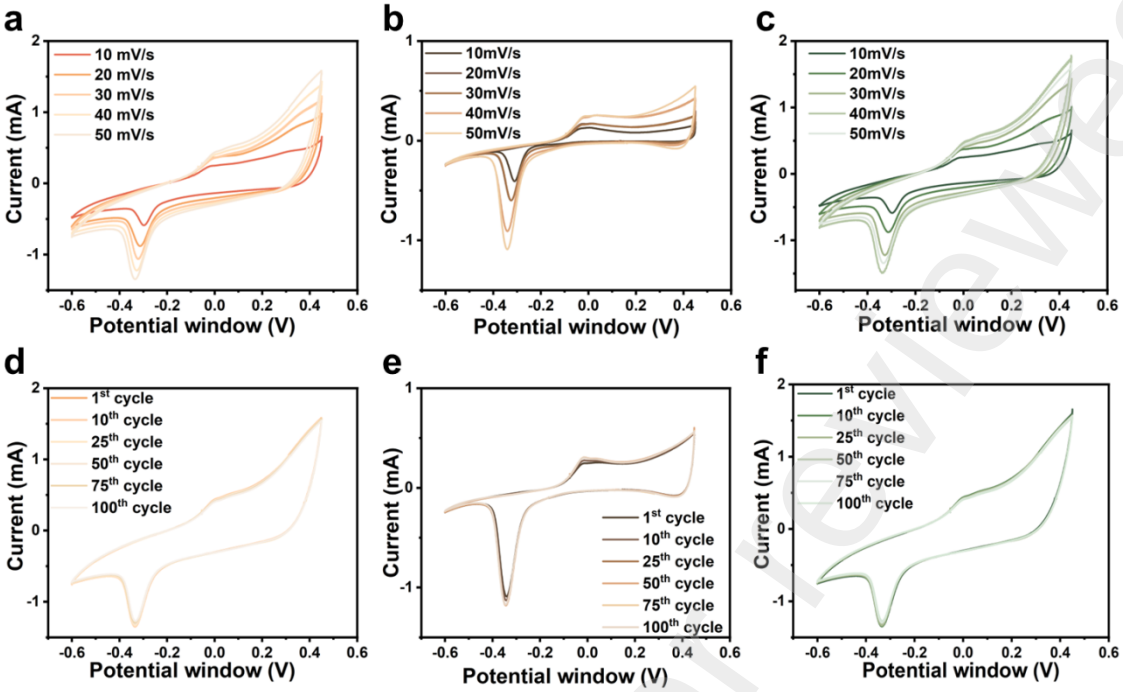

Figure 5. Cyclic voltammograms (CVs) of NMC samples, synthesized using the sol–gel (SG, a, d), solid-state (SS, b, e), and green synthesis (GS, c, f) methods. (a–c) CV curves recorded at different scan rates, ranging from 10 to 50 mV/s. (d–f) CV curves measured over multiple cycles (1st to 100th).

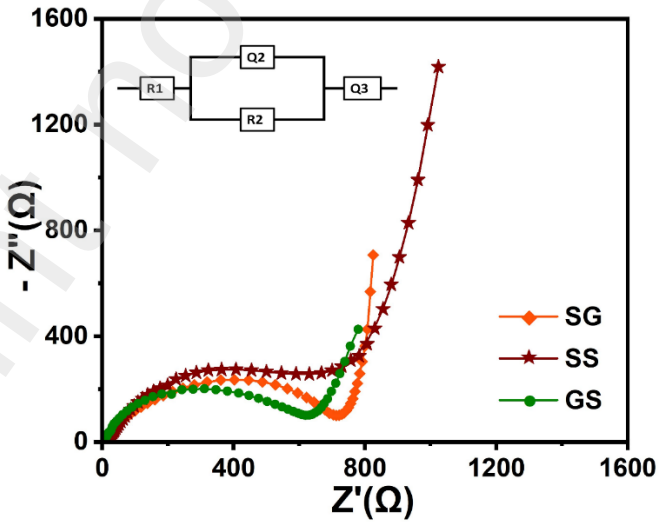

Figure 6. Nyquist plots of NMC electrodes synthesized using the sol–gel (SG), solid-state (SS), and green synthesis (GS) methods. The inset shows the equivalent-circuit model used for fitting.

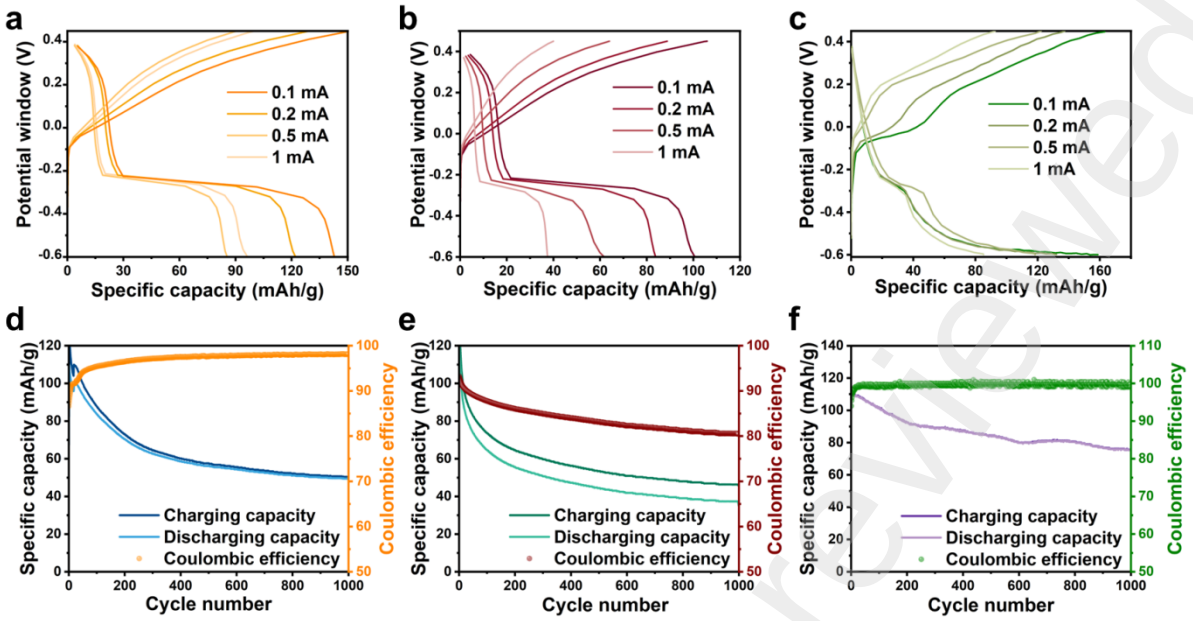

Figure 7. Galvanostatic charge–discharge (GCD) profiles (a–c) and long-term cycling performance (d–f) of NMC electrodes, synthesized using the sol–gel (SG), solid-state (SS), and green synthesis (GS) methods. GCD curves were measured at current densities ranging from 0.1 to 1 A/g. The cycling stability was evaluated over 1000 cycles with corresponding Coulombic efficiency.

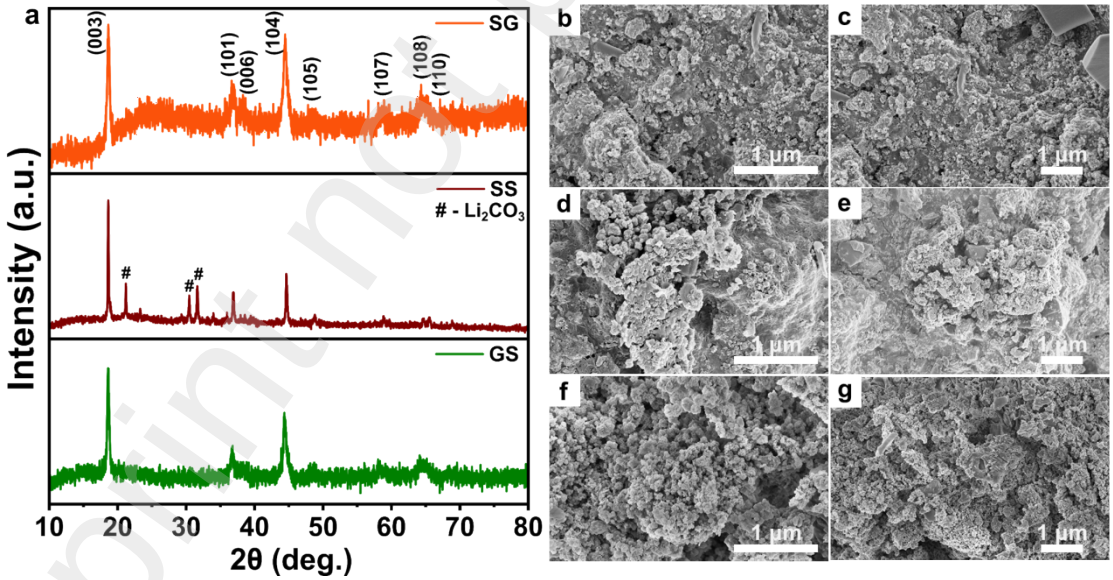

Figure 8. (a) Ex situ XRD patterns and (b–g) SEM images of NMC electrodes synthesized using the sol–gel (SG), solid-state (SS), and green synthesis (GS) methods after 1000 cycles.